Water Resources Research

RESEARCH ARTICLE
10.1029/2020WR027332

Influence of Radiation on Evaporation Rates: A Numerical Analysis

K. Heck[1], E. Coltman[1], J. Schneider[2], and R. Helmig[1]

[1]Institute for Modelling Hydraulic and Environmental Systems, Department of Hydromechanics and Modelling of Hydrosystems, University of Stuttgart, Stuttgart, Germany, [2]Agrosphere Institute, IBG-3, Forschungszentrum Jülich GmbH, Jülich, Germany

Key Points:
- We demonstrate the influence of radiation on evaporation rates
- The influence of surface undulations on radiation and evaporation is analyzed
- Comparison with experimental data shows the importance of interface processes

Correspondence to:
K. Heck,
Katharina.Heck@iws.uni-stuttgart.de

Citation:
Heck, K., Coltman, E., Schneider, J., & Helmig, R. (2020). Influence of radiation on evaporation rates: A numerical analysis. *Water Resources Research*, *56*, e2020WR027332. https://doi.org/10.1029/2020WR027332

Received 13 FEB 2020
Accepted 18 SEP 2020
Accepted article online 22 SEP 2020

Abstract We present a fully coupled soil-atmosphere model that includes radiation in the energy balance of the coupling conditions between the two domains. The model is able to describe evaporation processes under the influence of turbulence, surface roughness, and soil heterogeneities and focuses specifically on the influence of radiation on the mass and energy transport across the soil-atmosphere interface. It is shown that evaporation rates are clearly dominated by the diurnal cycle of solar irradiance. During Stage-I evaporation maximum temperatures are regulated due to evaporative cooling, but after a transition into Stage-II evaporation, temperatures rise tremendously. We compare two different soil types, a coarser, sandy soil and a finer, silty soil, and analyze evaporation rates, surface temperatures, and net radiation for three different wind conditions. The influence of surface undulations on radiation and evaporation is analyzed and shows that radiation can lead to different local drying patterns in the hills and the valleys of the porous medium, depending on the height of the undulations and on the direction of the Sun. At last a comparison of lysimeter measurement data to the numerical examples shows a good match for measured and calculated radiation values but evaporation rates are still overestimated in the model. Possible reasons for the discrepancy between measurement and model data are analyzed and are found to be uncertainties about the parameters close to the interface, which are decisive for determining evaporation rates.

1. Introduction

Evaporation from porous surfaces can have a major effect on city climate (Saneinejad et al., 2012); it can influence climate model predictions (Seneviratne et al., 2006), and on a smaller scale understanding the processes influencing evaporation rates from bare soil is crucial for many agricultural applications such as water management and tillage cycles (Davin et al., 2014; Vanderborght et al., 2017). Under natural conditions numerous different processes influence evaporation rates, for example, wind speed, radiation, or surface roughness.

Radiation plays a crucial role by supplying the necessary energy for the phase change of liquid water to water vapor and therefore is an important factor in the surface energy balance. A general surface energy balance for bare soil is denoted by (e.g., Brutsaert, 1982; Monteith, 1981; Penman & Keen, 1948)

$$R_n = L_e E + H + G, \tag{1}$$

where the incoming net radiation, R_n, is split up at the surface into latent heat, $L_e E$, a ground heat flux, G, and a sensible heat flux into the atmosphere, H.

A more indirect influence of radiation on evaporation rates is the dependency of various processes and parameters on temperature such as diffusion coefficients, densities, and viscosities. At the same time radiation is influenced by other processes and properties of the atmosphere and the soil as well. Surface roughness can lead to different albedo values of the soil (Matthias et al., 2000), water vapor in the atmosphere can lead to more adsorption of incoming light (e.g., Kiehl & Trenberth, 1997), and surface undulation, for example, occurring in tilled soil can prevent the Sun from reaching the soil surface equally.

Several models are available that are able to describe evaporation with different levels of complexity, especially regarding simplifications made for the coupling conditions between the soil and the atmosphere.

Vanderborght et al. (2017) give a thorough review of the capabilities and differences of these models. They conclude that for heterogeneous surfaces, it is necessary to investigate evaporation with a fully coupled model, describing flow and transport of mass and energy in the porous medium and the free flow. For homogeneous surfaces and soils, it is concluded that simpler relations suffice, for example, reduction to a 1-D model. In some of these models radiation is included in the energy balance but a complete analysis of the influence of radiation in a fully coupled soil-atmosphere model is to our knowledge still missing. In Fetzer et al. (2017) it is shown that for heterogeneous soils without radiation, lateral heat fluxes, which are neglected in 1-D models, can have a substantial impact on evaporation rates.

To overcome the above mentioned missing detailed analysis of the influence of radiation on mass and energy transport across the porous-medium free-flow interface, we present a fully coupled soil-atmosphere model, which is able to describe evaporation depending on the above mentioned processes. The model is based on previous work by Mosthaf et al. (2014) and Fetzer et al. (2016) and extends their model concept with a radiation concept.

We discuss and analyze three numerical examples, highlighting the importance of radiation and energy transport on evaporation rates under natural conditions. The first example shows evaporation from a flat soil with varying wind speeds, comparing the behavior of two different soil types. A second example demonstrates how surface undulations change radiation and evaporation and how a diurnal cycle of the Sun leads to different drying patterns during the day. At last we compare numerical results to experimental data obtained from lysimeters of the TERENO SoilCan Selhausen test site (Zacharias et al., 2011).

2. Model Concept

Investigating coupled free-flow porous-medium processes needs a proper description of the porous medium and the free flow. Additionally, the two domains need to be coupled by suitable coupling conditions. In the following the equations for both domains and the coupling conditions are described. Radiation is included as an extra coupling condition which is described in section 2.3.1.

2.1. Porous Medium

Flow and transport of water and air in a porous medium can be described by a mass balance with a multiphase Darcy's law (Helmig, 1997) as the momentum balance. To describe evaporation in a natural system, we balance the two components *water* and *air* in the liquid and the gaseous phase. *Air* is here considered as a component with a fixed composition of nitrogen and oxygen and no water vapor ("dry" air). The transport of the component *water* is then described in the second balance equation for *water* in vapor and liquid form. In a general formulation with the phases α and components κ this leads to

$$\frac{\partial}{\partial t}\left[\sum_{\alpha}\phi S_{\alpha}\varrho_{\alpha}X_{\alpha}^{\kappa}\right]+\nabla.\left[\sum_{\alpha}(X_{\alpha}^{\kappa}\varrho_{\alpha}\mathbf{v}_{\alpha}-j_{\mathrm{diff}}^{\kappa})\right]=\sum_{\alpha}q_{\alpha}^{\kappa}. \tag{2}$$

The mass fraction of each component κ in a phase α is denoted by X_{α}^{κ}, the saturation of each phase by S_{α}, the density of the fluid by ϱ_{α}, and the porosity of the porous medium by ϕ. The source/sink term for each component in each phase is denoted by q_{α}^{κ}. The velocity $\mathbf{v}_{\alpha}$ can be written as

$$\mathbf{v}_{\alpha}=\frac{k_{r,\alpha}K}{\mu_{\alpha}}(\nabla p_{\alpha}-\varrho_{g}\mathbf{g}). \tag{3}$$

K describes the intrinsic permeability of the soil, $k_{r,\alpha}$ the relative permeability, μ the dynamic viscosity of the fluid, and p_{α} the phase pressure. The diffusive transport can be described by Fick's law, which is valid in a binary system when Knudsen effects do not play a role, with

$$j_{\mathrm{diff}^{\kappa}}=D_{pm,\alpha}^{\kappa}\varrho_{\alpha}\nabla X_{\alpha}^{\kappa}. \tag{4}$$

The effective diffusion coefficient in a porous medium $D_{pm,\alpha}^{\kappa}$ is different from the molecular diffusion coefficient D_{α}^{κ} in a fluid due to tortuosity τ and porosity. Here, the relationship by Millington and Quirk (1961) is used to relate tortuosity, porosity, and saturation with the molecular diffusion coefficient to obtain the effective diffusion coefficient.

We assume a local thermodynamic equilibrium in the porous medium. Saturations, S, and the mass fractions, X_α^κ, of the components in each phase add up to one. For a two-phase system, with the wetting phase denoted by the subscript, w, and the nonwetting phase by, n, that leads to the constraints $S_w + S_n = 1$, $\sum_\kappa X_w^\kappa = 1$ and $\sum_\kappa X_n^\kappa = 1$. Dalton's law and Raoult's law are used to calculate phase compositions. Additionally, a relationship between saturation and capillary pressure needs to be employed, for example, van Genuchten (1980). Evaporation and radiation are highly nonisothermal processes, which means that an energy balance for the porous medium needs to be solved:

$$\frac{\partial}{\partial t}\left[\sum_\alpha (\phi \varrho_\alpha u_\alpha S_\alpha) + (1-\phi)\,\varrho_s c_s T_{pm}\right] - \nabla.\left[\sum_\alpha (\varrho_\alpha h_\alpha \mathbf{v}_\alpha) + \lambda_{\text{eff}} \nabla T_{pm})\right] = q^h. \tag{5}$$

The effective thermal conductivity of the soil λ_{eff} depends on all present phases and can be described by an effective relationship. We use the correlation proposed by Somerton et al. (1974). h_α describes the enthalpy (J) of a fluid phase α and u (J) the internal energy of the fluid phase with $u_\alpha = h_\alpha - p_\alpha/\varrho_\alpha$. c_s denotes the specific heat capacity of the solid material. The velocity of the fluid $\mathbf{v}_\alpha$ is described by Darcy's law, same as in the mass balance. q^h describes the source/sink term.

2.2. Free Flow

Depending on wind speed laminar or turbulent flow, behavior can occur under natural conditions. To capture turbulent flow, we use the Reynolds-averaged Navier-Stokes (RANS) equations and a k-ω model as closure relations for the eddy viscosity (Wilcox, 2006, 2008). The time-averaged terms in the RANS equations in the following are denoted by a bar (e.g., $\bar{\mathbf{v}}$). A total mass balance for the single-phase free flow is

$$\frac{\partial\left(\varrho_g\right)}{\partial t} + \nabla \cdot \left(\varrho_g \bar{\mathbf{v}}_g\right) = 0 \tag{6}$$

and the momentum balance of the RANS equations is given by

$$\frac{\partial(\varrho_g \bar{\mathbf{v}}_g)}{\partial t} + \nabla \cdot (\varrho_g \bar{\mathbf{v}}_g \bar{\mathbf{v}}_g^{\mathrm{T}}) - \nabla \cdot ((\mu_g + \mu_t)(\nabla \bar{\mathbf{v}}_g + \nabla \bar{\mathbf{v}}_g^{\mathrm{T}})) + \nabla \bar{p}_g - \varrho_g \mathbf{g} = 0. \tag{7}$$

The eddy viscosity μ_t is calculated by a k-ω model with k as the kinetic energy and ω as the turbulence frequency:

$$\mu_t = \frac{k}{\omega}\varrho_g. \tag{8}$$

The mass balance for a component κ in the gas phase g can then be described by

$$\frac{\partial\left(\varrho_g X_g^\kappa\right)}{\partial t} + \nabla \cdot \left(\varrho_g \bar{\mathbf{v}}_g X_g^\kappa - (D^\kappa + D_t)\varrho_g \nabla X_g^\kappa\right) - q^\kappa = 0. \tag{9}$$

The eddy diffusivity D_t is related to the eddy viscosity by the turbulent Schmidt number Sc_t:

$$D_t = \frac{\mu_t}{\mathrm{Sc}_t \varrho_g}. \tag{10}$$

Additionally, an energy balance is necessary:

$$\frac{\partial(\varrho_g u_g)}{\partial t} + \nabla.(\varrho_g h_g \bar{\mathbf{v}}_g) + \sum_\kappa \nabla.(h_g^\kappa j_{g,\mathrm{ff,diff}}^\kappa) - \nabla.((\lambda_g + \lambda_t))\nabla T) = 0. \tag{11}$$

The eddy thermal conductivity can be derived from the eddy viscosity with the turbulent Prandtl number Pr_t and the specific heat capacity $c_{p,g}$:

$$\lambda_t = \frac{\mu_t c_{p,g}}{Pr_t}. \tag{12}$$

2.3. Coupling Conditions

The interface conditions are based on the assumption of local thermodynamic equilibrium as described in Mosthaf et al. (2014) and Fetzer et al. (2016). We refer to that publications for more details.

As we assume a sharp interface between the two domains that does not store mass, momentum, or energy, all mass leaving one domain has to instantaneously appear in the other. Continuity of fluxes can be written as follows:

$$[(\varrho_g \bar{\mathbf{v}}_g) \cdot \mathbf{n}]^{\mathrm{ff}} = -[(\varrho_g \mathbf{v}_g + \varrho_w \mathbf{v}_w) \cdot \mathbf{n}]^{\mathrm{pm}} \tag{13}$$

with $\mathbf{n}$ as the interface normal vector (always pointing out of the respective domain).

For the tangential momentum the coupling condition is set according to the Beavers-Joseph-Saffman condition with α_{BJ} as the Beavers-Joseph coefficient, $\mathbf{t}_i$ as a tangential vector and the shear stress tensor $\bar{\tau}_{\mathrm{eff}} = (\mu_{\mathrm{g}} + \mu_{\mathrm{t}})(\nabla \bar{\mathbf{v}}_g + \nabla \bar{\mathbf{v}}_g^{\mathrm{T}})$:

$$\left[\left(\bar{\mathbf{v}}_g - \frac{\sqrt{(\mathbf{K}\mathbf{t}_i) \cdot \mathbf{t}_i}}{\alpha_{BJ}\mu_g} \bar{\tau}_{\mathrm{eff}} \mathbf{n}\right) \cdot \mathbf{t}_i\right]^{\mathrm{ff}} = 0, \quad i \in \{1, .., dim - 1\}. \tag{14}$$

For the normal part of the momentum balance the coupling condition is

$$[((\varrho_g \bar{\mathbf{v}}_g \bar{\mathbf{v}}_g^T - \bar{\tau}_{\mathrm{eff}} + \bar{p}_g \mathbf{I})\mathbf{n}) \cdot \mathbf{n}]^{\mathrm{ff}} = [p_g]^{\mathrm{pm}} \tag{15}$$

with the identity matrix $\mathbf{I}$.

For the components continuity of fluxes leads to

$$\left[(\varrho_g X_g^\kappa \bar{\mathbf{v}}_g + j_{\mathrm{diff,\,ff,\,t}}) \cdot \mathbf{n}\right]^{\mathrm{ff}} = -\left[\left(\sum_\alpha \left(\varrho_\alpha X_\alpha^\kappa \mathbf{v}_\alpha + j^\kappa_{\alpha,\,\mathrm{diff,\,pm}}\right)\right) \cdot \mathbf{n}\right]^{\mathrm{pm}}. \tag{16}$$

For the energy coupling the flux condition is as follows:

$$\left[\left(\varrho_g h_g \bar{\mathbf{v}}_g + \sum_\kappa h_g^\kappa j^\kappa_{\mathrm{g,diff}} + \lambda_g \nabla T\right) \cdot \mathbf{n}\right]^{\mathrm{ff}} = R_n - \left[\left(\sum_\alpha \left(\varrho_\alpha h_\alpha \mathbf{v}_\alpha + \sum_\kappa h_\alpha^\kappa j^\kappa_{\alpha,\mathrm{diff}}\right) - \lambda_{\mathrm{pm}} \nabla T\right) \cdot \mathbf{n}\right]^{\mathrm{pm}}. \tag{17}$$

R_n denotes the net radiation explained in the following.

2.3.1. Radiation

In natural systems, the Sun emits shortwave radiation, which is partially reflected in the atmosphere or at the soil surface and partially absorbed in the soil. Additionally, a part of the radiation is transferred back into the atmosphere as longwave radiation. That partitioning of the radiation highly depends on the surface albedo, surface emissivity, surface temperature, and atmospheric temperatures and emissivity near the surface. The part of the incoming radiation that is absorbed by the soil either supplies energy for the phase change of liquid water to vapor is transmitted back to the atmosphere by conduction or longwave radiation, or it leads to higher soil temperatures and more ground heat flux, G. All these processes happen in close proximity to the soil-atmosphere interface, which makes it necessary to include a proper description of that interface.

Previous work to include radiation in a coupled soil-atmosphere model has been done by, for example, Yamanaka et al. (1998) or Novak (2010). They use transfer functions to describe evaporation rates and do not analyze the behavior of the atmosphere coupled to a porous medium explicitly.

We follow a different approach, including net radiation directly in the coupling conditions at the interface between soil and atmosphere. This enables us to further investigate the sensitively coupled soil-atmosphere interface where free-flow turbulence, surface roughness, and solar radiation will alter the evaporative mass and heat fluxes.

To describe the longwave and shortwave radiation, a relationship by Brutsaert (1982) and Novak (2010) is used:

$$R_n = S_{irr}(1 - \alpha_s) + \sigma_B \epsilon_s (\epsilon_\alpha T_\alpha^4 - T_s^4), \tag{18}$$

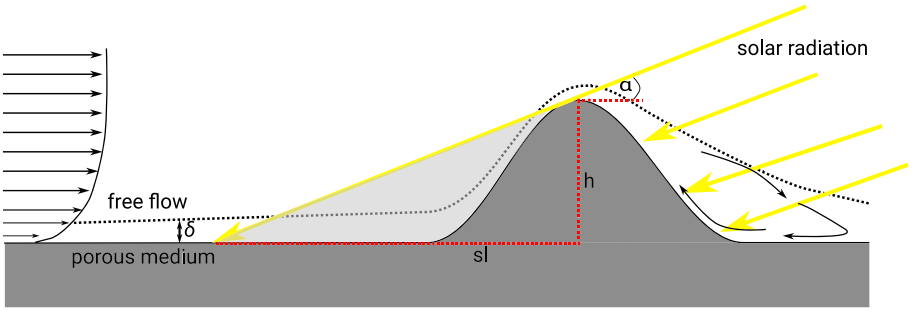

Figure 1. A sketch of the shadow length, sl, in a 2-D system, dependent on the angle of irradiance, α, and the height of the hill, h. Additionally, the evolving viscous sublayer, δ, over a small hill is displayed.

with

S_{irr} = solar irradiance,
σ_B = Stefan-Boltzmann constant,
ϵ_α = atmospheric emissivity,
α_s = surface albedo,
ϵ_s = soil surface emissivity,
T_α = atmospheric temperature,
T_s = soil surface temperature.

The Stefan-Boltzmann constant is given with $5.67 \cdot 10^{-8}\,\mathrm{W/(m^2\,K^4)}$. The soil surface temperature and the atmospheric temperature at the soil surface are primary variables of the model. For the other parameters additional relations need to be found.

Solar irradiance S_{irr} naturally varies daily with no radiation during the night and a varied radiation during the day, peaking at midday. Either measurement data can be used, or as in this study, a function describing the daily variation of solar irradiance (Yamanaka et al., 1998):

$$S_{irr} = 800 \cos\left(2\pi \frac{t+12}{24}\right) \tag{19}$$

for $6 < t < 18$ hr and $S_{irr} = 0$ for $t > 18$ and $t < 6$. This diurnal variation matches a solar irradiance variation for areas where there is 12 hr of sunlight. It is only valid for flat surfaces where the Sun is at a 90° angle at midday. To include the angle of the interface, this equation is adapted to

$$S_{irr} = 800 \cos\left(2\pi \frac{t+12}{24} + \gamma\right) \tag{20}$$

with γ as the angle of the surface. For an angle of 0° this function reaches its maximum at 12 p.m. and for an upward angle of 45° at 9 in the morning. Of course, the maximum value of $800\,\mathrm{W/m^2}$ can be adapted depending on the location and climate conditions of interest. For cloudy days and more distance to the equator that value is declining.

The atmospheric emissivity can be expressed as a function of the atmospheric temperature, T_α, and the vapor pressure, p_g^w (in hPa) (Brutsaert, 1982) with

$$\epsilon_\alpha = 1.24\left(\frac{p_g^w}{T_\alpha}\right)^{\frac{1}{7}}. \tag{21}$$

The soil surface emissivity and soil surface albedo are also parameters that can be taken from measurements. They both depend highly on soil types and saturation of the soil. In Novak (2010) parameters for the surface emissivity and surface albedo are given depending on the soil moisture content. These parameters are further used in this study. Surface albedo has a major influence on evaporation rates and surface temperatures (Davin et al., 2014), but the focus of this work is investigating evaporation under the influence of radiation not focusing on different albedo values.

Additionally, when considering a full daily circle and nonflat surfaces, the surface's shadow can prevent solar radiation from reaching the soil surface. This means that the length of the shadow has to be calculated which for a 2-D system can be done with geometrical considerations as sketched in Figure 1. The shadow length, sl, can then be calculated with $\mathrm{sl} = \tan(90° - \alpha) \cdot h$ and α as the angle of irradiance, which can be

Table 1
Material Properties of the Soil Used in the Three First Examples

Parameter	Sandy soil	Silty soil	
n	8	1.32	(−)
α	6.37E−4	4.28E−5	(1/Pa)
Snr	0.01	0.029	(-)
Swr	0.005	0.057	(-)
ϕ	0.41	0.35	(-)
K	2.65E−10	1.08E−12	(m^2)
c_s	790	790	(J/(kg K))
λ_s	2.8	2.8	(W/(m K))
ρ_s	2,600	2,600	(kg/m^3)

deducted from the calculation of the solar irradiance. In case an area is in the shadow the solar irradiance is then set to 0. As previously described this calculation of net radiation is then included in the coupling condition of the energy balance.

3. Discretization and Implementation

The mathematical model is discretized by an implicit Euler method in time. The free flow part is approximated in space by a finite-volume staggered grid scheme (Marker and Cell [MAC] scheme) with a second-order approximation of the convective term. The porous medium is discretized by a finite-volume cell-centered two-point flux scheme. More details for that implementation can be found in, for example, Fetzer (2018).

The equations are implemented in the numerical software framework DuMu^x (Flemisch et al., 2011; Heck et al., 2019; Koch et al., 2020). All code relevant to obtaining the numerical examples can be found under Gitlab (git.iws.uni-stuttgart.de/dumux-pub/Heck2020a).

4. Comparison and Analysis

In the first two test cases we use the same sandy soil, for which van-Genuchten parameters, porosity, and permeability are summarized in Table 1. Additionally, the first example compares the drying behavior of

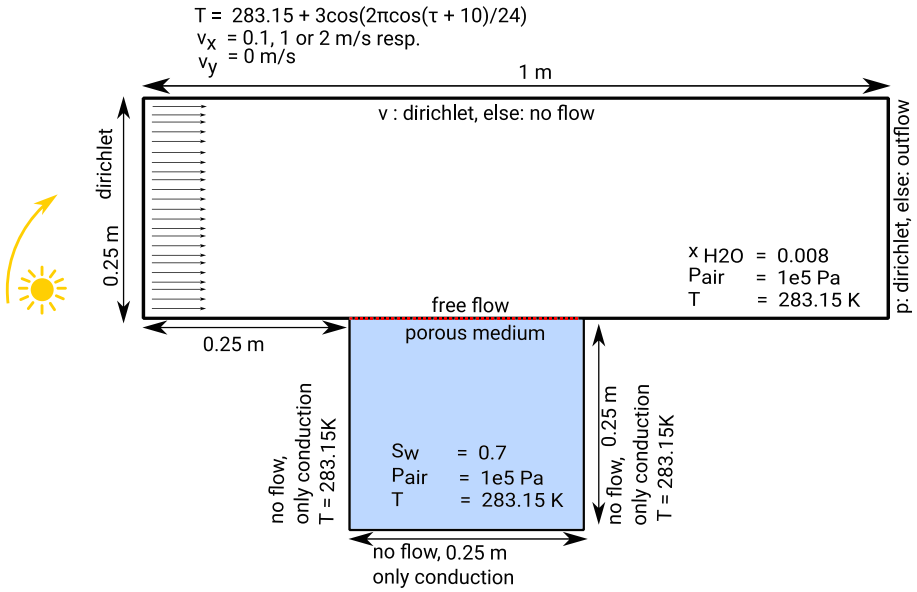

Figure 2. Initial and boundary conditions, for example, one to three, with τ as the time in hours. The problem is discretized with 100 cells in the horizontal direction and 60 in vertical direction with a refinement toward the interface.

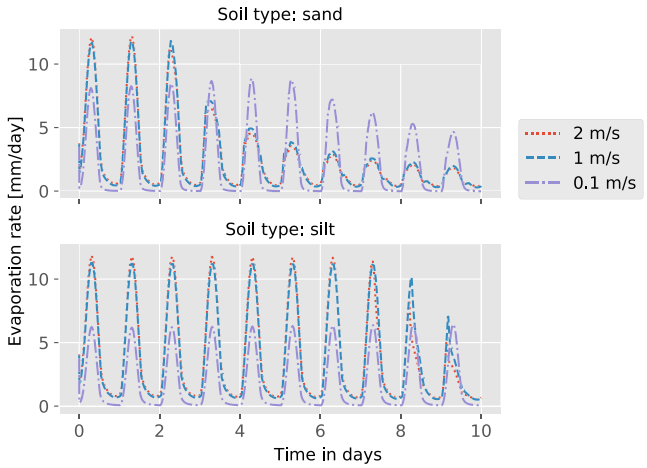

Figure 3. Evaporation rates over 10 days for two different soil types as simulated in the described setup. The shape of the curves is dominated by the diurnal cycle of radiation. Still, differences in wind velocities are visible.

the sandy soil to a finer silty soil; these parameters can also be found in the table. In the last example spatial parameters are taken from measurement data to match the soil properties from the experimental setup. Porosity and permeability are held constant throughout.

4.1. Influence of Radiation on Surface Temperature and Evaporation Rates

The first example shows a flat porous medium with an adjacent free-flow channel as shown in Figure 2. The setup is chosen to mimic an experimental facility where the porous medium is a tank filled with either one of the two soil types. The tank is placed at the base of a controlled atmospheric free-flow channel. Wind flows from left to right continuously, and the mass fraction of water vapor is constant at the inflow. Radiation varies with a diurnal cycle and the inflow air temperatures vary accordingly. The function for air temperature depending on time of the day can be found similarly in Yamanaka et al. (1998). The simulation starts at 6 in the morning ($\tau = 6$). All the sides of the tank are closed for fluid flow and allow only conduction. Three wind velocities are compared: one case, where flow conditions are laminar with a low velocity of 0.1 m/s, and two cases, where flow conditions are turbulent, with velocities of 1 and 2 m/s.

In Figure 3, it can be observed that, although the shape of the evaporation flux is governed by the diurnal cycle of the Sun, the amount of evaporation is governed by the availability of water. During the first three days, the peak evaporation rates from the sandy soil reach the same magnitude, as the capillary flow is high enough to satisfy the evaporative demand. That stage of drying is commonly referred to as Stage-I evaporation (e.g., Lehmann et al., 2008). Afterward, during the transition to Stage-II evaporation, the evaporation rates drop significantly for the two higher wind speeds as the porous medium dries. Water saturation at the interface decreases toward the residual saturation and evaporation rates are diffusion limited. Daily peaks in evaporation rates can still be seen due to solar radiation. When the temperature in the soil rises, this leads to a high water vapor content in the soil and therefore high diffusive fluxes. For the lowest wind speed, the transition into Stage-II evaporation is slower. For the silt-type soil, evaporation rates remain in Stage-I evaporation much longer; the transition into Stage-II evaporation begins under the two higher velocities 8 days after the beginning of the test. The laminar test case remains in Stage-I evaporation. Noteworthy is the lower peak evaporation rates of the silt compared to the sandy soil for the laminar case. This is due to the different water saturations of the two soil types and therefore also different effective thermal conductivities of the soil, which depend on water saturation. For the higher wind velocities, the saturation at the interface is lower, even for the silty soil. In comparison to the higher exchanges driven by the higher wind velocities, the effects of soil saturation is less noticeable.

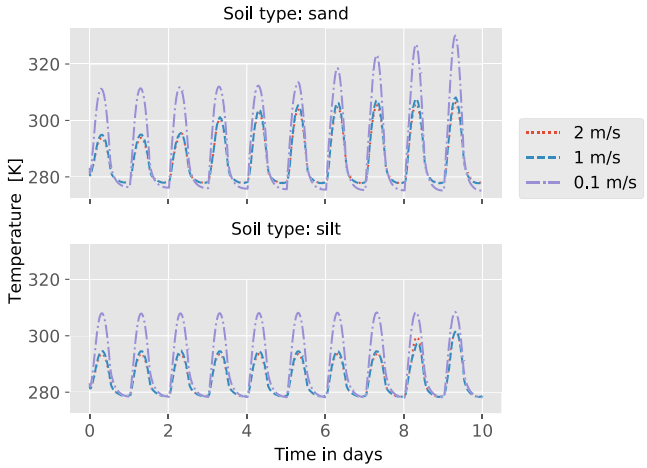

Figure 4. Simulated surface temperatures of the porous medium over 10 days. After a transition into Stage-II evaporation peak temperatures begin to rise.

Comparing wind velocities shows that during Stage-I evaporation higher wind speeds lead to higher evaporation rates, but the shape of the curve is clearly dominated by radiation. The transition into the diffusion-limited Stage-II evaporation is faster for higher flow velocities as water saturations at the interface decrease faster as well. During Days 7–10, it can be seen for the sandy soil that evaporation rates are nearly the same for the two higher velocities, they are governed by diffusion and not by wind velocities.

That transition into Stage-II evaporation can also be seen in the surface temperature curve in Figure 4. After the drop in evaporation rates the surface temperatures of the porous medium begin to rise, as the evaporative cooling has a minor effect. This can be observed for both soil types, although at different times due to the slower drying of the silt-type soil. The highest wind velocity shows the fastest transition into Stage-II evaporation. On the fourth day, the simulation with the sandy soil shows that for wind velocities of 2 m/s evaporation rates are lower than for 1 m/s.

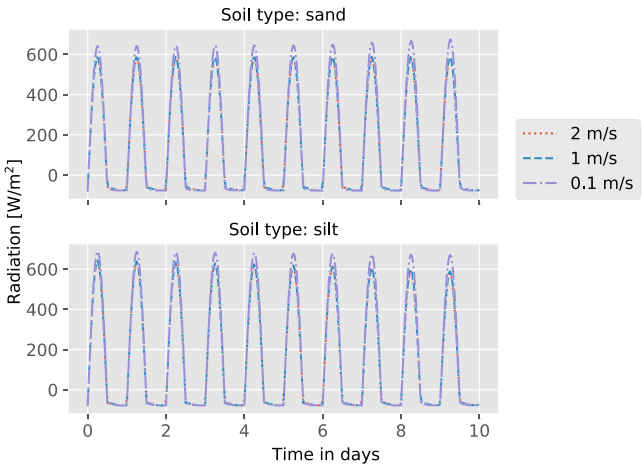

Figure 5. Simulated net radiation over 10 days for two different soil types. A small decline in net radiation is visible for silty soil during transition to Stage-II evaporation.

Still surface temperatures show no significant difference, which indicates that higher ground heat flux or conductive heat exchange with the atmosphere mitigate the effect of less evaporative cooling.

The laminar test case continuously shows higher surface temperatures than the other two test cases. This can be attributed to the lower evaporation rates and therefore lower evaporative cooling, and also to the reduced conductive heat exchange with the atmosphere, due to higher atmospheric temperatures than in the turbulent cases. For the laminar case less mixing with the cooler atmosphere leads to higher temperatures in the boundary layer, which reduces the conductive heat exchange with the warmer soil. For the same reason, lower wind speeds lead to less longwave radiation, which also enhances peak temperatures. Comparing the different soil types, it can be seen that the silty soil continuously has lower peak temperatures. This can be explained by the higher evaporation rates; when the sandy soil is already in Stage-II evaporation, the silty soil still is in Stage-I evaporation, which leads to more evaporative cooling. At the same time the higher water saturations at the interface lead to higher effective thermal conductivity and more ground heat flux, which can additionally lower temperatures at the interface.

Net radiation does not vary substantially during transition from Stage-I to Stage-II evaporation, but a small decline in net radiation over the 10 days is visible for the silty soil (see Figure 5). This decline can be explained by the higher surface temperatures during the transition into Stage-II evaporation, which lead to more longwave radiation. Additionally, soil albedo is higher when saturations are lower. During drying of the silty soil, the reduction in saturation decreases the net radiation. For the sandy soil, this is less visible. Here, the saturations are low from the beginning, which mitigates the effect of changing albedo values with saturation. The laminar test case continuously shows a higher peak in net radiation, which is most likely due to less longwave radiation, as atmospheric temperatures are higher with less mixing in the atmosphere. Radiation is highest at midday while evaporation rates and surface temperatures have their daily highest peak at 2 p.m. in the afternoon.

To analyze if the heat provided to the soil due to solar radiation also substantially influences fluid parameters like density, viscosity, and diffusion coefficients and to assess how these changes reflect on the evaporation rate, we show a laminar and turbulent test case in Appendix A, where we selectively neglect temperature dependence of that parameters. The setup uses the same boundary conditions as given in Figure 2. It can be seen that peak evaporation rates are very similar for all cases and the changes in viscosity, density, or diffusion coefficients due to temperature changes do not alter evaporation rates substantially. Only in the laminar test case neglecting temperature influences on density and diffusion coefficients leads to lower peak evaporation rates. This can be explained by an enhanced mixing in the boundary layer when densities and diffusion coefficients are higher due to higher temperatures.

4.2. Surface Undulations

Soil under natural conditions is seldom completely flat. For example, when one imagines a tilled field, it is more likely that the surface has some undulations and is in general rather rough. Verma and Cermak (1974), Haghighi and Or (2015), and Gao et al. (2018) investigate surface undulations and their effect on evaporation rates, omitting the influence of radiation. Key findings are that surface undulations can lead to both higher or lower evaporation rates compared to a flat surface, highlighting the complexity of soil-water evaporation from nonflat surfaces.

Surface undulations affect the evaporation rates in various ways: (I) They increase the surface area, leading to a higher exchange area for evaporation. (II) They reduce the overall wind flow velocities in the valleys, leading to less mixing and increased water vapor content in the valleys, reducing evaporation rates. (III) Higher surface undulations might reduce the water availability in the hills as capillary forces can be too weak to overcome gravity. An interesting aspect in that regard is the different flow behavior on the sides of the hills turned toward and away from the wind. As evaporation rates in the viscous sublayer are diffusion limited, the thickness of this layer is an important factor in determining evaporation rates. Obstacles can influence that layer tremendously. Around the obstacle, boundary layers will detach and reattach downstream, depending

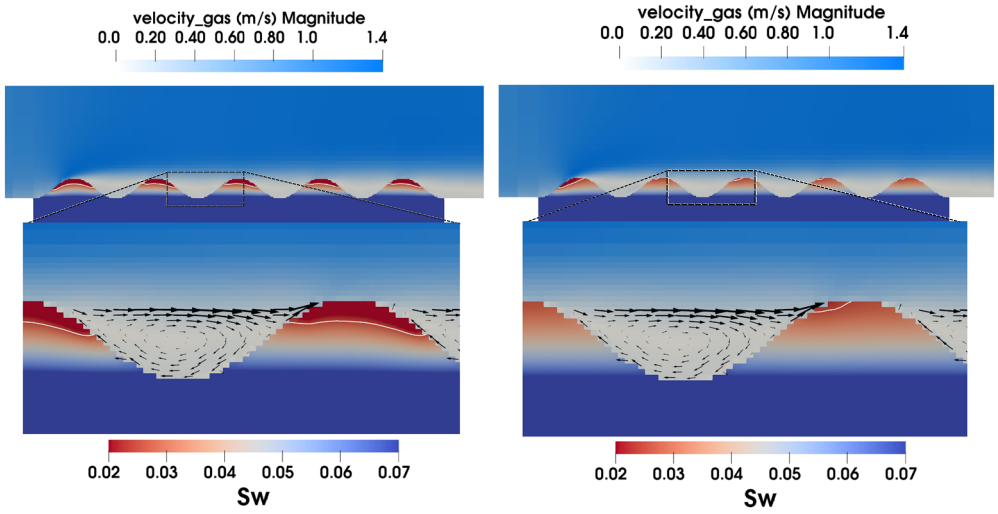

Figure 6. Simulated velocity distribution in the atmosphere and saturation distribution in the porous medium. The white line in the zoomed picture shows the value $Sw = 0.025$. Above that line saturations are lower than that value. At 4 p.m. (left) and at 10 p.m (right). At night saturations are higher as evaporation is limited. The lowest values can be observed on the wind facing slopes.

on the geometry of the surface and the wind velocity. In the valleys, eddies occur and an increase in water vapor locally decreases evaporation rates. Figure 1 shows a sketch of that behavior of the viscous sublayer over a small hill.

Including radiation in such a model poses a few additional challenges: (I) The shadow length has to be properly accounted for, which reduces solar radiation in the valleys depending on the angle of the Sun. (II) The angle of the surface toward the Sun needs to be accounted for in the calculation of solar irradiance.

To assess the influence of surface undulations, different setups are compared:

- 5 cm hills: The setup with the same boundary and initial conditions as in Figure 2 is analyzed with five hills with 5 cm height.
- 2 cm hills: The same setup is analyzed for 2 cm high hills, and the differences between the different heights are compared.
- Reversed flow direction: A case where the wind flow direction in relation to the diurnal cycle of the Sun is reversed (Sun rises on the right and sets on the left) is analyzed in comparison to the previously described case.

The first setup with surface undulations describes a system where the wind and the Sun match, rising and flowing from left to right. The Sun rises on the left at 6 in the morning and sets at 6 in the evening on the right side. When neglecting radiation, one would expect that evaporation rates are highest on the left facing sides of the waves, which are turned toward the wind, due to the thinned boundary layer thickness as sketched in Figure 1. Including radiation can change that behavior as the local temperature rise due to radiation influences the evaporation rate more than wind velocity.

Figure 6 shows the velocity distribution in the atmosphere and the saturation in the porous medium at 4 p.m. and at night at 10 p.m. for a setup with five hills. It can be seen, that in both cases, flow velocities are higher at the top of the hills on the side facing the wind. In the night, without radiation, this location at the top of the hills is then also the point where saturations are lowest due to the highest evaporation rate. During the afternoon, the Sun shines directly on the sides turned away from the wind, heating up the soil and leading to higher evaporation rates on those sides, which can be observed from the lower values for saturation on those sides. Additionally, it can be observed that in this stage of drying, water saturations in the hills are higher at night than during the day, which means capillary forces are still high enough to resaturate the dried surface layer.

Figure 7 shows evaporation rates, the average net radiation at the interface, and the average surface temperature for 2 and 5 cm high hills. When the Sun rises in the morning, at first net radiation is higher for smaller

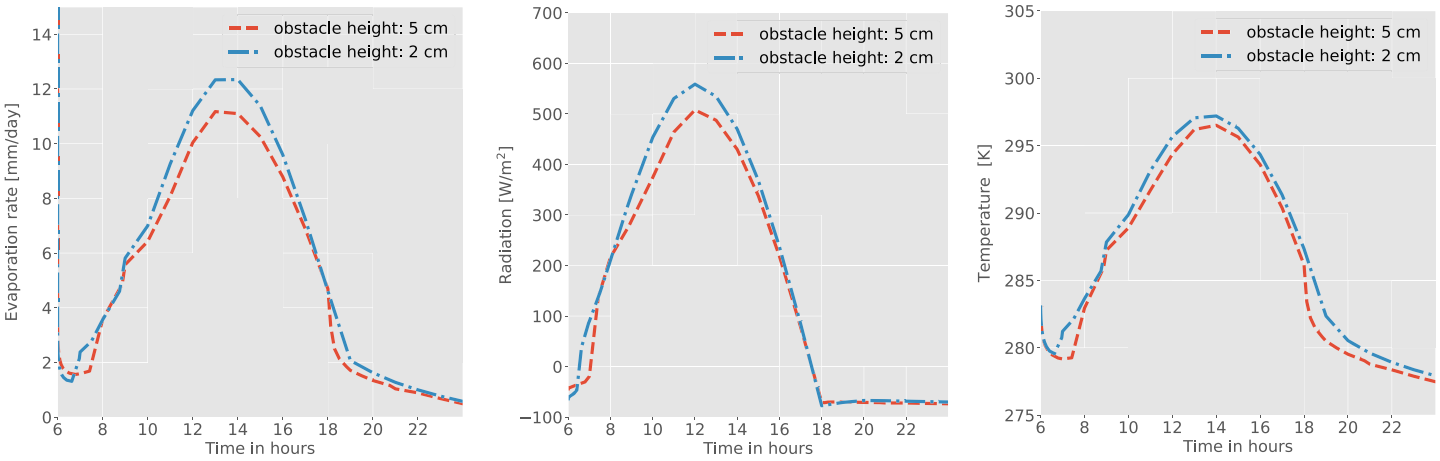

Figure 7. Simulated evaporation rates (left), net radiation (middle), and average temperature at the interface (right) for different heights of surface undulations.

undulations, as shadow lengths are shorter for smaller undulations. This is also reflected in higher evaporation and higher temperatures, especially visible at 7 a.m. Later in the day, when shadow lengths are shorter, that effect is dominated by the higher surface area of the higher undulations as more surface area is directly exposed to the Sun. Around 9 a.m. the 5 cm high hills start to dry locally, when capillary forces are not high enough to continuously supply water, which leads to the sharper change in evaporation rates at that time.

At 12 p.m. obstacles lead to a smaller peak in net radiation, as the surfaces are more inclined. Therefore, at midday the Sun is not perpendicular to the whole surface and net radiation is smaller.

Due to increased surface area with higher undulations the integrated energy input is higher for higher undulations, though. This can be seen in the evaporation rates. Locally, the evaporation rates (mm/day) are lower for higher obstacles, which is influenced by the lower net radiation. In contrast, integrated over the interface area, mass loss of water is greater for the higher obstacles due to the increased surface area, which can be seen in Appendix B where average saturation during drying is shown for both surface undulations and it can be observed that higher obstacles lead to lower values in average saturation.

The changes in surface temperature due to the difference in height of the hills reflect the above described effects, which have a contrary influence on temperatures. The higher energy input due to more surface area increases the temperature, but at the same time, the higher mass loss of water leads to a cooling of the surface. Here, it can be seen that surface temperatures are lower for higher obstacles.

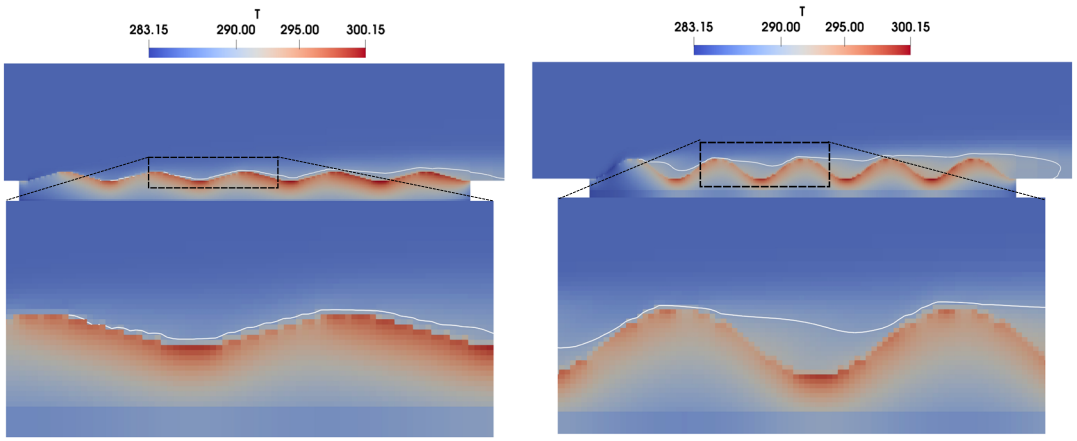

Figure 8. Simulated temperature distribution in the atmosphere and in the soil at 12 p.m. The white line shows a temperature of $T = 289.15$ K. Below that line, values are higher. For 2 cm high hills (left) and for 5 cm hills (right). For 5 cm high hills, less mixing with the atmosphere leads to higher temperatures in the valleys.

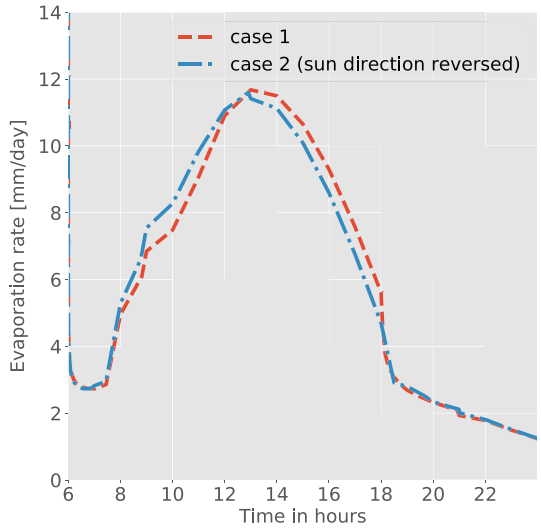

Figure 9. Simulated evaporation rates for two scenarios over the course of one day. Case 1: the Sun rises on the left and sets on the right and Case 2: the reversed case. Only a small variation in evaporation rates between the two cases is visible.

Although the average surface temperature is higher for lower hills, the atmospheric temperature is still higher in the valleys of the higher undulations due to less mixing, which can be seen in Figure 8. Here, the valleys between the 5 cm hills are clearly influenced by the eddy, forming in the valley. Temperatures are highest on the left side of the valley, because the warm air is rotated in that direction. For the 2 cm high hills, that effect is not dominating, but the temperatures are similar on both sides of the hill, a bit higher even on the right side of the valley, as this is the side, that was exposed to the Sun in the morning.

As previously described, another setup was implemented to test if changing the flow direction in comparison to the Sun changes evaporation rates substantially. The case where the Sun rises on the left and sets on the right is in the following referred to as Case 1 and the reversed case (Sun rises on the right side and wind flows from left to right) as Case 2. To get a better distinction between the effects of wind velocity and radiation, the wind velocity is increased to 2 m/s.

Comparing these two cases in Figure 9, there is only a small variation in overall evaporation rates in the tested parameter set. Evaporation rates in the morning are higher for Case 2 but lower in the afternoon. That can be explained by considering that both radiation and wind velocities raise evaporation rates. For Case 1, in the morning the Sun shines on the left sides of the small hills, the same side exposed to the most wind. Locally that side dries considerably faster, there are spots where the capillary forces cannot supply enough water and there is a transition into Stage-II evaporation, which lowers the overall evaporation rates. The reversed case splits the evaporative driving forces for evaporation radiation and wind velocity in the morning to different surface sides of the hill. This leads overall to higher evaporation rates as fewer spots dry out completely.

This is supported by analyzing the local pattern of water saturation, which can be found in Appendix B. Saturations for Case 1 are lower on the left side of the hills while for Case 2 the saturations are low at the right side as well, which shows that broader spread in local evaporation. In the afternoon, evaporation rates for the reversed case are lower, as the Sun then shines directly on the left sides of the hills, which are already dryer due to the exposure to wind. Overall, it can be seen that these effects for the tested case are not dominant and the cumulative mass loss over the whole day is comparable for both cases. This result is of course very dependent on initial saturations and soil properties, when saturations are higher and the soil does not dry out at all, evaporation rates will not be influenced by the location of radiation compared to wind velocities.

4.3. Comparison With Experimental Data

To assess the capabilities of the model, it is important to compare the results with experimental data. Here, the model is compared to data measured from soil lysimeters in the TERENO SoilCan Selhausen test site at the Forschungszentrum Jülich, Germany (50° 52′ 8.6″N, 06° 27′ 57.2″E), which is part of the TERENO Rur observatory (Zacharias et al., 2011). A measurement period of three sunny days in September 2016 after a rainfall event is selected. The days are chosen so that no precipitation occurred in that time to only analyze evaporation.

The spatial parameters and measurements selected belong to the soil Sauerbach (Sb-10). Additionally, wind velocity measurements, air temperatures, and relative humidity data measured in 2 m height are used as input data for the boundary conditions of the free flow. Figure 10 shows a sketch of the experimental setup with the location of measurement and the boundary and initial conditions for the simulation setup. Only the first two horizons of the soil are modeled and a Dirichlet condition is set at the bottom of the porous medium domain to mimic the recharge from the lower soil layers. During the measurement time, measured values lower than the first 50 cm do not show substantial changes, which justifies that choice of boundary conditions.

Figure 11 shows the measured atmospheric parameters in 2 m height over the three days. These measured parameters are used as input data uniformly on the left side of the free-flow domain for the turbulent free flow as well as for the developing boundary layer. The soil parameters used as input data are given in Table 2.

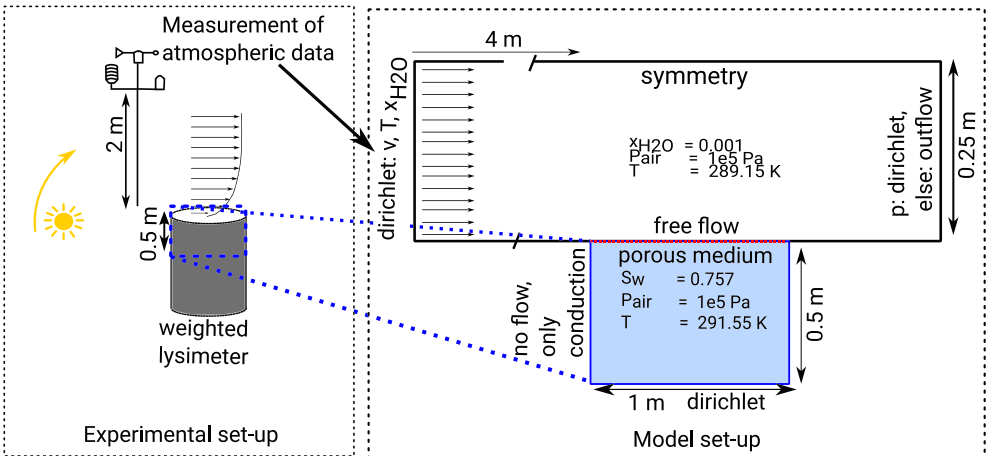

Figure 10. Experimental setup of the lysimeter with measurement of the atmospheric parameters in 2 m height and initial and boundary conditions for the model setup. The problem is discretized with 75 cells in the horizontal direction and 80 in vertical direction with a refinement toward the interface. The velocity measured at 2 m height is set as a block profile on the left side. The free flow domain is extended at the front to provide a better flow profile before reaching the measurement site.

It would also be possible to use radiation data as input for the coupling conditions but the previously described model for radiation is used instead, and the results are compared. The only change to the radiation calculation is to lower the maximum solar irradiance from 800 to 600 W/m^2, as 800 W/m^2 is a more suitable value for locations closer to the equator (e.g., Geiger et al., 2008). This also agrees more with the measured maximum values for net radiation.

The TERENO SoilCan project offers different data sets to compare and analyze the model results on a lysimeter scale under natural conditions. Still, such a comparison poses some challenges especially when trying to compare the measured data to a model, which requires detailed information about properties close to the free-flow porous-medium interface. Measurements close to that interface are difficult to obtain.

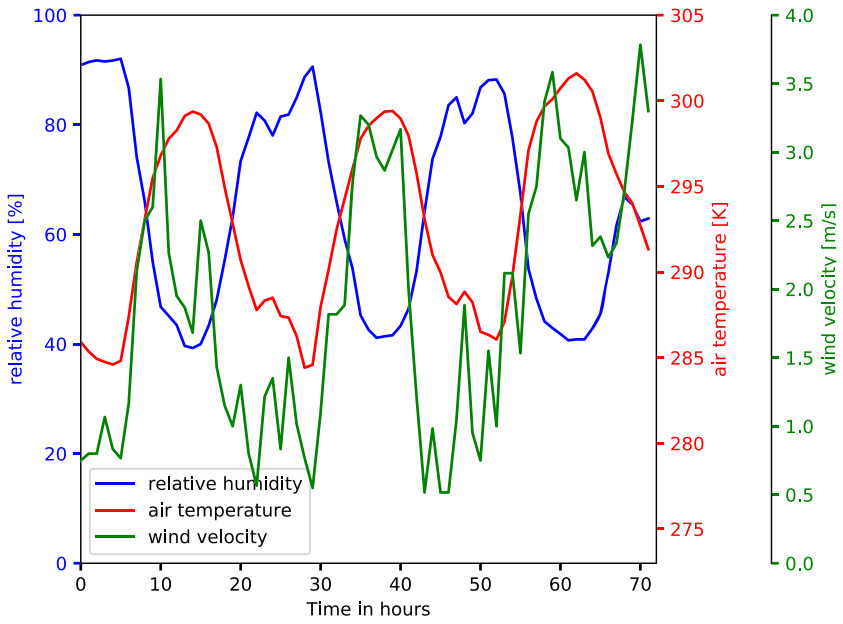

Figure 11. Measurement data obtained at the measurement site in 2 m height and set as input parameters on the left side of the free-flow domain.

Table 2
Spatial Parameters for the First Two Horizons From Experimental Data for the Soil Sb-10

Parameter	Horizon 1	Horizon 2	
n	1.5	1.59	(-)
α	7.54332E−5	6.6E−5	(1/Pa)
Snr	0.00814	0.073	(-)
Swr	0.18	0.14	(-)
ϕ	0.376	0.398	(-)
K	1.68E−12	7.7E−14	(m^2)

Sensitive parameters determining evaporation rates are, that is, relative humidity, initial water saturation, initial surface temperature, and soil parameters close to the interface. To assess the influence of these parameters, four test cases, analyzing different influences, are discussed:

(a) Unchanged setup: Measurement values as obtained in the experiment are set as boundary conditions, and the spatial parameters, as analyzed for the first 50 cm, are set for the modeled domain.
(b) Extended porous medium: Relative humidity is set as a boundary condition at the inlet on the left side of the free flow. In reality, that quantity is measured at 2 m height. This value does not contain information about the relative humidity in the boundary layer, which is decisive for the evaporation rates. The wind flows over an open field before reaching the measurement site; therefore, it is very likely that the boundary layer has an increased water vapor content than the value that is measured at 2 m height, which is set as a boundary condition. To quantify that effect, an additional test case is run where the porous-medium domain and the free-flow domain are both extended on the upwind side by 10 m. This means that before reaching the actual measurement site, the wind already flows over a 10 m long porous medium with the same conditions as the measurement site so that when it reaches the site, the air is more enriched with water vapor. Of course, that does not replicate reality; as the soil type next to the lysimeters is different, there might be vegetation disturbing the flow field and in general the conditions are unknown. Regardless, this makes effects of the incoming boundary layer relative humidity on the evaporation rate more realistic and is a good setup to see the influence of that value.
(c) Initial saturation and temperature at the interface: Another uncertainty of the model is choosing the right initial saturation and temperature, which is measured first at 10 cm depth (30 cm for temperature) in the soil and not right at the interface. Close to the interface these values influence evaporation rates tremendously. To assess this uncertainty, a test case is set up where, in the first centimeter of the soil, the initial temperature is reduced by 4°C and the initial water saturation is lowered to 0.7. As before, these values are chosen to see the sensitivity of that parameters and not to replicate the true conditions.
(d) Spatial parameters in the top layer: Various studies (e.g., Dimitrov et al., 2015) suggest that soil parameters close to the interface are very sensitive to the treatment of the soil. The Sb-10 soil was tilled and afterward smoothed again by raking before the start of the measurement, which is why it is likely that hydraulic parameters of the soil at the interface can be very different from the initially measured values for the first horizon. To test that hypothesis, the van-Genuchten parameters for the upper 3 cm are varied for one test case to Snr = 0.2, α = 7.54E−4 (1/Pa), and n = 1.6.

Figure 12 shows a comparison of measured net radiation and evaporation rates and simulated values. It is visible that the quite simple approach to model net radiation already gives quite good results for radiation rates for all tested cases. The differences between the cases stem from the varying evaporation rates and therefore different surface temperatures leading to different longwave radiation.

For evaporation rates a higher discrepancy between experiment and simulation can be seen. During night, the evaporation rates deviate not substantially. However, during the day predicted evaporation rates for the unchanged setup (Case a) are around 3 times higher than the measured values.

It can be observed that the extension of the porous medium by 10 m (Case b) leads to a drastic reduction in evaporation rates. This proves that measurements of the relative humidity closer to the interface between soil and atmosphere are necessary to assess if the model then represents the experimental measurements

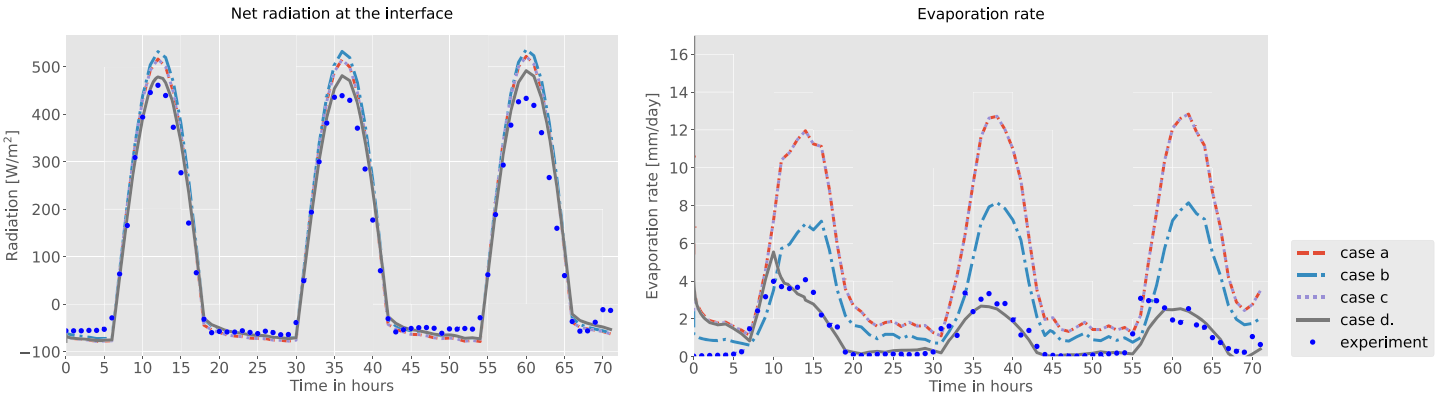

Figure 12. Comparison of simulated net radiation (left) and evaporation rates (right) with measured values for the four different tested cases. The best fit between measurement and simulation can be seen for Case (d).

more closely. The extension of the porous medium by 10 m only serves as a tool to analyze the sensitivity of that hypothesis.

The initial surface temperature and initial water saturation (Case c) only influence evaporation rates in the beginning. After a few hours the initial values do not influence the overall result, especially as the given capillary pressure saturation relationship for Sb-10 allows capillary rise of water during the whole time. This process governs the water saturation at the interface, and the soil does not dry out during the whole simulated time, meaning evaporation conditions are continuously in Stage-I evaporation and governed by atmospheric conditions rather than soil conditions.

Changing the spatial parameters of the first 3 cm (Case d) changes the overall result tremendously, as with the chosen spatial parameters the capillary pressure is not high enough to supply water to the first layer and evaporation becomes diffusion limited. With this change in parameters, the measured and simulated evaporation rate are within the same order of magnitude. This indicates that indeed the treatment of the soil changed the parameters of the first layer, as with the previously set parameters (Case c) a drying of the soil to a diffusion limited evaporation range was not possible.

A comparison of water saturation and temperatures with experimental results in 10 cm depth, respectively 30 cm depth for the temperature, can be found in Appendix C for Case (a) and Case (d), as they show the most deviation in prediction of evaporation rates. It can be seen that saturations do not vary substantially over time for the experiment as well as the simulations. For the case without any change in parameters (Case a) a diurnal cycle in saturation is visible, while when the first layer of soil is dry and not hydraulically connected to the lower layers (Case d), then water saturation does not show this pattern anymore. As the experimental results also show some diurnal variations, it is likely that in reality the soil is still partially hydraulically connected to the upper layer. Temperatures in the experiment show a higher variation between night and day than predicted in both cases. Case (d) shows a better match for peak temperatures, as in Case a the higher evaporation rates lead to more evaporative cooling, therefore underestimating the peak temperatures. During night temperatures of Case (d) are higher than experimental values, though. This can be attributed to uncertainties in thermal conductivities, which depend on saturation. As saturation also vary between the experiment and simulation, this difference is expected.

This analysis shows that the model is able to capture relevant physical processes. All variations in parameters show the expected behavior and can be physically explained. It is found that the soil and atmospheric conditions close to the interface are especially critical in determining evaporation rates. Still, a comparison to the experimental data is challenging as these values close to the interface are difficult to determine.

For further analysis of the system another step would be to include the surface roughness of the tilled soil as that can lead to major changes in evaporation rates as well (Fetzer et al., 2016).

5. Conclusion

We present a fully coupled soil-atmosphere model including radiation, which is able to describe and analyze evaporation rates under natural conditions. The first example shows that radiation clearly influences the

diurnal cycle of evaporation, with highest evaporation rates between 1 and 2 p.m. The temperature profile is also clearly dominated by the diurnal cycle of the Sun, but evaporative cooling still has a major effect. During Stage-I evaporation, the highest temperatures during the day remain constant, while after the transition into Stage-II evaporation the maximum value raises daily. This indicates that during a heat wave when there is no precipitation, the cooling of the soil during the night is not enough to cool down the temperatures sufficiently. Higher wind velocities lead to higher peaks in evaporation during Stage-I evaporation and a faster transition into Stage-II evaporation. A comparison of two different soil types shows a fast transition to Stage-II evaporation and high temperature rise for sandy soil, while the silty soil stays in Stage-I evaporation longer and surface temperatures do not rise as fast.

The second example shows the influence of surface undulations on radiation and evaporation. It is shown that during a diurnal cycle, the drying behavior in the hills is immensely influenced by the Sun. During the night, the highest evaporation rates can be observed at the sides facing the wind, as their locations have the smallest boundary layer thickness. During the day, highest evaporation rates can be observed at the location where the Sun shines perpendicular to these locations as the temperature increase and therefore higher vapor pressure dominates over the evaporation process. An analysis of the height of the undulations shows that locally radiation is lower for higher surface undulations, leading to lower evaporation rates. On the contrast, integrated over the whole surface area, higher obstacles lead to a higher surface area and the cumulative mass loss of water is higher. This shows that the height of surface undulations and therefore the length of surface area clearly influence the drying of the soil, which shows that tillage of the soil can change evaporation rates drastically. Changing the wind direction in relation to the cycle of the Sun does not change evaporation rates substantially. In the daily cycle evaporative fluxes are slightly higher in the morning, when the Sun shines on the hills facing away from the wind, but lower in the afternoon, where the Sun shines on the already drier sides of the obstacles turned toward the wind. This has no major effect on cumulative rates though.

Comparing the model results to experimental data shows that the model is able to produce good matches for net radiation. Regarding evaporation rates, there is still a discrepancy between measured and simulated values. To asses that discrepancy, various parameters are varied and their influence is analyzed. The results show that the effects of the parameters can all be physically explained, and the model is able to capture their influence. It is shown that information about values close to the interface is necessary to get good model results. Major influences are seen for relative humidity values and spatial parameters close to the interface. To further assess the capabilities of the model, a more detailed comparison to measurement data is still necessary. A detailed analysis of the different components of net radiation could help in identifying missing links between experimental data and the model.

Appendix A: Analysis of Fluid Parameters

Here, evaporation rates for four different test cases under laminar and turbulent conditions are shown. This helps to analyze how evaporation rates are influenced by the changing fluid parameters due to a diurnal

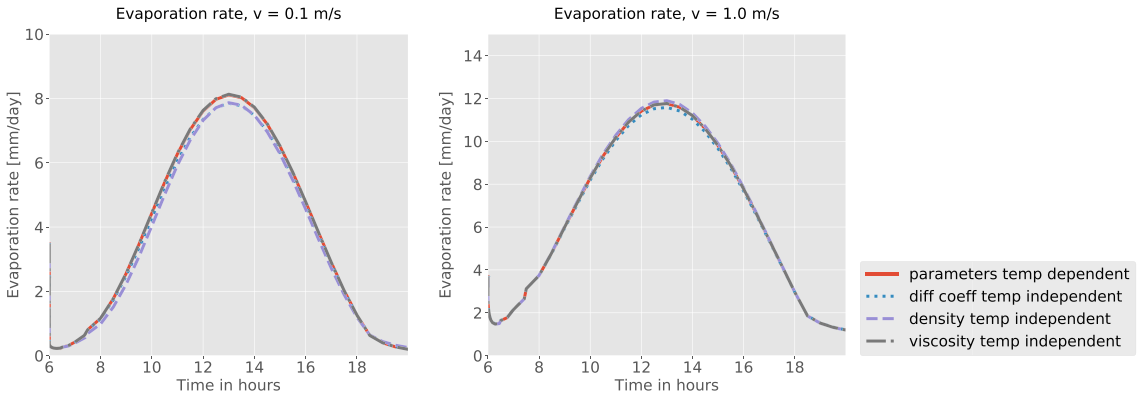

Figure A1. Evaporation rates of the different simulations runs where fluid parameters are selectively independent of temperature changes with a maximum wind velocity of 0.1 m/s (left) and 1 m/s (right).

cycle of radiation. In one case, all fluid parameters vary with temperatures changes while for the other three cases the influence of temperature on one of the parameters is neglected (Figure A1).

Appendix B: Analysis of Surface Undulations

Figure B1 supports the analysis of the influence of different heights of surface undulations on evaporation rates. It can be seen that the average water saturation in the porous medium decreases faster for higher undulations.

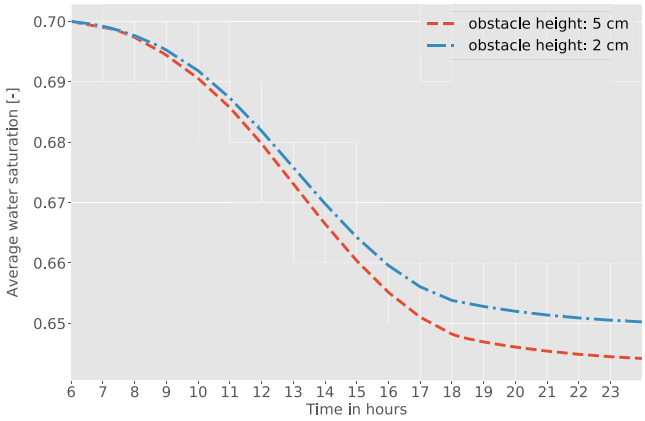

Figure B1. Average water saturation during one day of drying for different heights of surface undulations.

In Figure B2 water saturations in the porous medium are displayed for two cases with different angles of solar irradiance. In Case 1, the Sun rises on the left and sets on the right. In Case 2, this rotation is reversed. In the free flow the velocity magnitude can be seen.

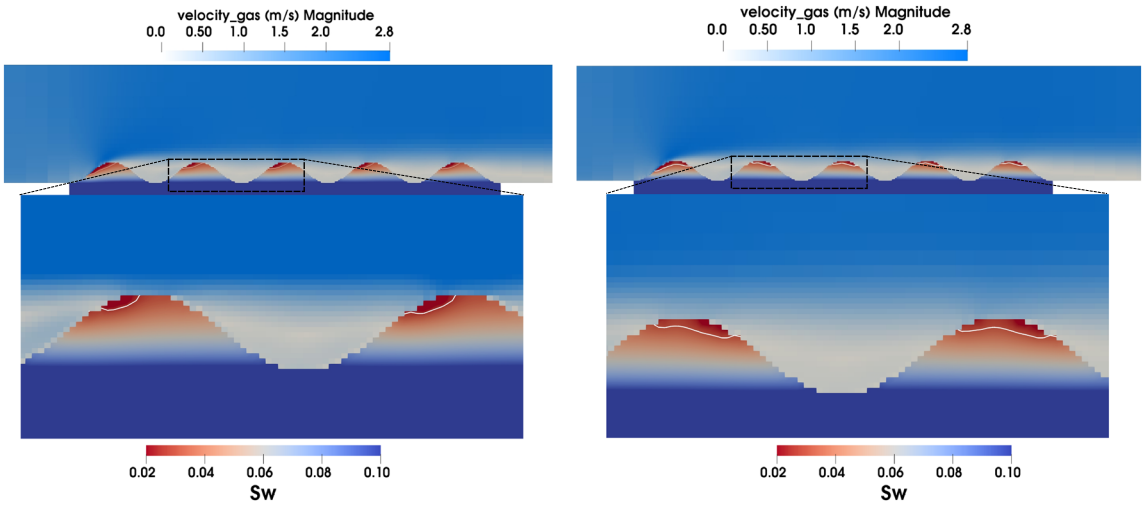

Figure B2. Saturation in the porous medium and velocity in the atmosphere for Case 1 (left) where the Sun rises on the left and sets on the right and Case 2 (right) with a reversed Sun direction, both at 9 a.m. The white line shows a saturation of $S = 0.03$. Above that line, saturation are lower.

Appendix C: Comparison With Experimental Data

Here, water saturations and temperatures comparing experimental data from the lysimeters and the simulations can be seen (Figure C1). Case (a) describes the simulation where the measured parameters are used throughout the whole domain, and Case (d) describes a setup where the first centimeters of the soil have different van-Genuchten parameters.

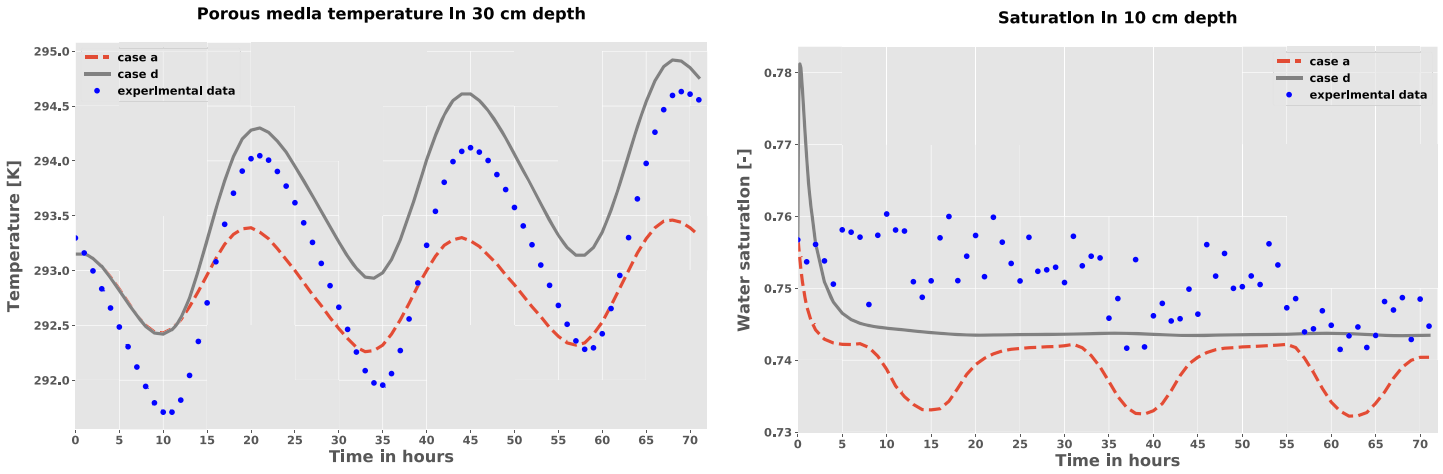

Figure C1. Comparison of water saturation in 10 cm depth and temperatures in 30 cm depth between experimental results and two simulation setups, where evaporation rates deviate the most.

Data Availability Statement

The data from the experimental measurements of the TERENO project (Zacharias et al., 2011) can be found under https://www.tereno.net/ for the TERENO SoilCan Selhausen test site at the Forschungszentrum Jülich, Germany. The observed days are 6 to 8 September 2016. All code relevant to obtaining the numerical examples is implemented in DuMu^x (Heck et al., 2019; Koch et al., 2020) and can be found under Gitlab (git.iws.uni-stuttgart.de/dumux-pub/Heck2020a).

Acknowledgments
This work was financially supported by the German Research Foundation (DFG), within the Collaborative Research Center on Interface-Driven Multi-Field Processes in Porous Media (SFB 1313, Project Number 327154368 - Project A02) and the DFG Research Group Satin 2531/14-1.

References

Brutsaert, W. (1982). *Evaporation into the atmosphere*. Netherlands: Springer Netherlands.

Davin, E. L., Seneviratne, S. I., Ciais, P., Olioso, A., & Wang, T. (2014). Preferential cooling of hot extremes from cropland albedo management. *Proceedings of the National Academy of Sciences*, *111*(27), 9757–9761. https://doi.org/10.1073/pnas.1317323111

Dimitrov, M., Vanderborght, J., Kostov, K., Debecker, B., Schulze Lammers, P., Damerow, L., & Vereecken, H. (2015). Soil hydraulic parameters of bare soil plots with different soil structure inversely derived from L-band brightness temperatures. *Vadose Zone Journal*, *14*, 1–23. https://doi.org/10.2136/vzj2014.09.0133

Fetzer, T. (2018). Coupled free and porous-medium flow processes affected by turbulence and roughness: Models, concepts and analysis.

Fetzer, T., Smits, K. M., & Helmig, R. (2016). Effect of turbulence and roughness on coupled porous-medium/free-flow exchange processes. *Transport in Porous Media*, *114*(2), 395–424. https://doi.org/10.1007/s11242-016-0654-6

Fetzer, T., Vanderborght, J., Mosthaf, K., Smits, K. M., & Helmig, R. (2017). Heat and water transport in soils and across the soil-atmosphere interface: 2. Numerical analysis. *Water Resources Research*, *53*, 1080–1100. https://doi.org/10.1002/2016WR019983

Flemisch, B., Darcis, M., Erbertseder, K., Faigle, B., Lauser, A., Mosthaf, K., et al. (2011). DuMux^x: Dune for multi- phase, component, scale, physics, ... flow and transport in porous media. *Advances in Water Resources*, *34*, 1102–1112. https://doi.org/10.1016/j.advwatres.2011.03.007

Gao, B., Davarzani, H., Helmig, R., & Smits, K. M. (2018). Experimental and numerical study of evaporation from wavy surfaces by coupling free flow and porous media flow. *Water Resources Research*, *54*, 9096–9117. https://doi.org/10.1029/2018WR023423

Geiger, B., Meurey, C., Lajas, D., Franchistéguy, L., Carrer, D., & Roujean, J.-L. (2008). Near real-time provision of downwelling shortwave radiation estimates derived from satellite observations. *Meteorological Applications*, *15*(3), 411–420. https://doi.org/10.1002/met.84

Haghighi, E., & Or, D. (2015). Evaporation from wavy porous surfaces into turbulent airflows. *Transport in Porous Media*, *110*(2), 225250. https://doi.org/10.1007/s11242-015-0512-y10.1007/s11242-015-0512-y

Heck, K., Ackermann, S., Becker, B., Coltman, E., Emmert, S., Flemisch, B., et al. (2019). Dumux 3.1.0. Zenodo, https://doi.org/10.5281/zenodo.3482428

Helmig, R. (1997). *Multiphase flow and transport processes in the subsurface: A contribution to the modeling of hydrosystems (environmental science and engineering)*. Berlin: Springer.

Kiehl, J. T., & Trenberth, K. E. (1997). Earth's annual global mean energy budget. *Bulletin of the American Meteorological Society*, *78*(2), 197–208. https://doi.org/10.1175/1520-0477(1997)078<0197:eagmeb>2.0.co;2

Koch, T., Gläser, D., Weishaupt, K., Ackermann, S., Beck, M., Becker, B., et al. (2020). Dumu^{x}3—an open-source simulator for solving flow and transport problems in porous media with a focus on model coupling. *Computers & Mathematics with Applications*. https://doi.org/10.1016/j.camwa.2020.02.012

Lehmann, P., Assouline, S., & Or, D. (2008). Characteristic lengths affecting evaporative drying of porous media. *Physical Review E*, *77*, 056309. https://doi.org/10.1103/PhysRevE.77.056309

Matthias, A., Fimbres, A., Sano, E., Post, D., Accioly, L., Batchily, A., & Ferreira, L. (2000). Surface roughness effects on soil albedo. *Soil Science Society of America Journal*, *64*, 1035–1041. https://doi.org/10.2136/sssaj2000.6431035x

Millington, R. J., & Quirk, J. P. (1961). Permeability of porous solids. *Transactions of the Faraday Society*, *57*, 1200. https://doi.org/10.1039/tf9615701200

Monteith, J. L. (1981). Evaporation and surface temperature. *Quarterly Journal of the Royal Meteorological Society*, *107*(451), 1–27. https://doi.org/10.1002/qj.49710745102

Mosthaf, K., Helmig, R., & Or, D. (2014). Modeling and analysis of evaporation processes from porous media on the rev scale. *Water Resources Research*, *50*, 1059–1079. https://doi.org/10.1002/2013WR014442

Novak, M. D. (2010). Dynamics of the near-surface evaporation zone and corresponding effects on the surface energy balance of a drying bare soil. *Agricultural and Forest Meteorology*, *150*(10), 1358–1365. https://doi.org/10.1016/j.agrformet.2010.06.005

Penman, H. L., & Keen, B. A. (1948). Natural evaporation from open water, bare soil and grass. *Proceedings of the Royal Society of London. Series A. Mathematical and Physical Sciences*, *193*(1032), 120–145. https://doi.org/10.1098/rspa.1948.0037

Saneinejad, S., Moonen, P., Defraeye, T., Derome, D., & Carmeliet, J. (2012). Coupled CFD, radiation and porous media transport model for evaluating evaporative cooling in an urban environment. *Journal of Wind Engineering and Industrial Aerodynamics*, *104-106*, 455–463. https://doi.org/10.1016/j.jweia.2012.02.006

Seneviratne, S. I., Lüthi, D., Litschi, M., & Schär, C. (2006). Land atmosphere coupling and climate change in Europe. *Nature*, *443*(7108), 205–209. https://doi.org/10.1038/nature05095

Somerton, W. H., Keese, J. A., & Chu, S. L. (1974). Thermal behavior of unconsolidated oil sands. *Society of Petroleum Engineers Journal*, *14*(05), 513–521. https://doi.org/10.2118/4506-pa

van Genuchten, M. T. (1980). A closed-form equation for predicting the hydraulic conductivity of unsaturated soils1. *Soil Science Society of America Journal*, *44*(5), 892. https://doi.org/10.2136/sssaj1980.03615995004400050002x

Vanderborght, J., Fetzer, T., Mosthaf, K., Smits, K. M., & Helmig, R. (2017). Heat and water transport in soils and across the soil-atmosphere interface: 1. Theory and different model concepts. *Water Resources Research*, *53*, 1057–1079. https://doi.org/10.1002/2016WR019982

Verma, S. B., & Cermak, J. E. (1974). Wind-tunnel investigation of mass transfer from soil corrugations. *Journal of Applied Meteorology*, *13*(5), 578–587. https://doi.org/10.1175/1520-0450(1974)013<0578:wtiomt>2.0.co;2

Wilcox, D. C. (2006). *Turbulence modeling for CFD (third edition)*. New York: D C W Industries.

Wilcox, D. C. (2008). Formulation of the *k-ω* turbulence model revisited. *American Institute of Aeronautics and Astronautics Journal*, *46*(11), 2823–2838.

Yamanaka, T., Takeda, A., & Shimada, J. (1998). Evaporation beneath the soil surface: Some observational evidence and numerical experiments. *Hydrological Processes*, *12*(13-14), 2193–2203. https://doi.org/10.1002/(SICI)1099-1085(19981030)12:13/14<2193::AID-HYP729>3.0.CO;2-P

Zacharias, S., Bogena, H., Samaniego, L., Mauder, M., Fuß, R., Pütz, T., et al. (2011). A network of terrestrial environmental observatories in Germany. *Vadose Zone Journal*, *10*(3), 955–973. https://doi.org/10.2136/vzj2010.0139